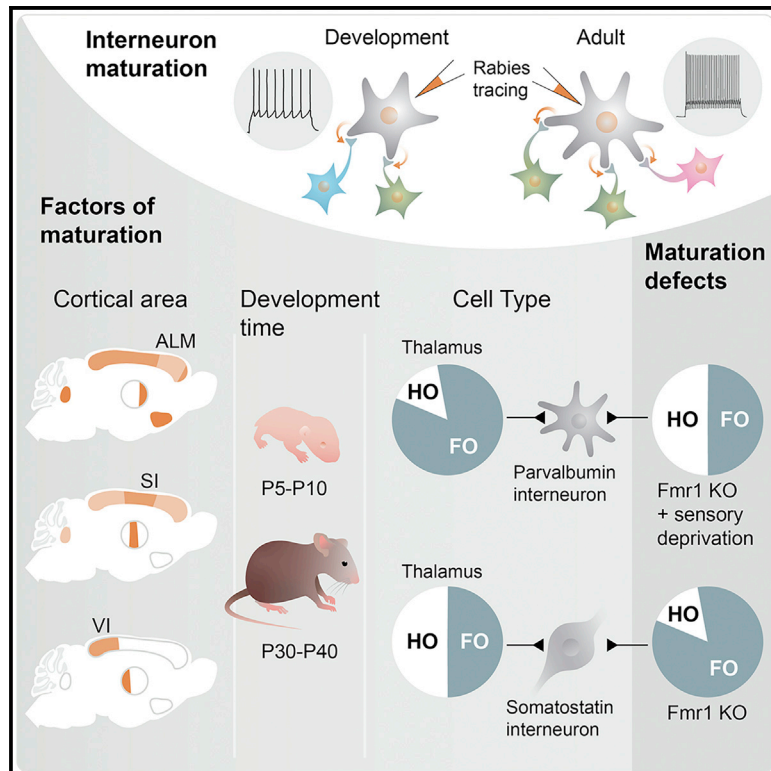# The organization and development of cortical interneuron presynaptic circuits are area specific

Graphical abstract

Authors
Gabrielle Pouchelon, Deepanjali Dwivedi, Yannick Bollmann, ..., Kimberly D. Ritola, Rosa Cossart, Gord Fishell

Correspondence
gordon_fishell@hms.harvard.edu

In brief
Using monosynaptic rabies tracing and physiology, Pouchelon et al. show that inputs to inhibitory interneurons primarily reflect their cortical location, which adjust those inputs through distinct dynamics during development, in accordance with cell type. Specific sets of the developmentally regulated inputs are disrupted by sensory deprivation or in Fmr1 KOs.

Highlights
- Monosynaptic rabies tracing and physiological properties reveal circuit maturation

- Inputs to inhibitory interneurons are primarily defined by their cortical location

- Cell types adjust their areal-specific inputs with distinct developmental dynamics

- Fmr1 KO and sensory deprivations induce specific sets of input maturation defects

CellPress

Resource

The organization and development of cortical interneuron presynaptic circuits are area specific

Gabrielle Pouchelon,[1,2] Deepanjali Dwivedi,[1,2,9] Yannick Bollmann,[3,6,9] Chimuanya K. Agba,[1,2,7] Qing Xu,[4] Andrea M.C. Mirow,[1] Sehyun Kim,[1] Yanjie Qiu,[1,2] Elaine Sevier,[1,2] Kimberly D. Ritola,[5,8] Rosa Cossart,[3] and Gord Fishell[1,2,10,*]

[1]Harvard Medical School, Department of Neurobiology, Boston, MA 02115, USA
[2]Broad Institute, Stanley Center for Psychiatric Research, Cambridge, MA 02142, USA
[3]Aix Marseille University, INSERM, INMED, Turing Center for Living Systems, Marseille, France
[4]Center for Genomics & Systems Biology, New York University Abu Dhabi, Abu Dhabi, UAE
[5]Janelia Research Campus, Howard Hughes Medical Institute, Ashburn, VA 20147, USA
[6]Current address: King's College London, London, UK
[7]Current address: UC San Diego, Department of Neuroscience, La Jolla, CA 92093, USA
[8]Current address: University of North Carolina at Chapel Hill, NC 27514, USA
[9]These authors contributed equally
[10]Lead contact
*Correspondence: gordon_fishell@hms.harvard.edu
https://doi.org/10.1016/j.celrep.2021.109993

SUMMARY

Parvalbumin and somatostatin inhibitory interneurons gate information flow in discrete cortical areas that compute sensory and cognitive functions. Despite the considerable differences between areas, individual interneuron subtypes are genetically invariant and are thought to form canonical circuits regardless of which area they are embedded in. Here, we investigate whether this is achieved through selective and systematic variations in their afferent connectivity during development. To this end, we examined the development of their inputs within distinct cortical areas. We find that interneuron afferents show little evidence of being globally stereotyped. Rather, each subtype displays characteristic regional connectivity and distinct developmental dynamics by which this connectivity is achieved. Moreover, afferents dynamically regulated during development are disrupted by early sensory deprivation and in a model of fragile X syndrome. These data provide a comprehensive map of interneuron afferents across cortical areas and reveal the logic by which these circuits are established during development.

INTRODUCTION

Our conscious perception of the world is rooted in the neocortex. Integration of sensory information and the generation of cognitive functions, such as motor planning or prediction, are processed in discrete cortical areas. Across all these regions, GABAergic parvalbumin (PV) and somatostatin (SST) cells, the two largest classes of cortical interneurons (cINs), occupy the deep layers of cortex and form local computational units that differentially gate information flow (Muñoz and Rudy, 2014). Within the anterolateral motor cortex (ALM) (Allen et al., 2017) PV and SST cINs contribute to motor planning, while in primary somatosensory cortex (S1) and the primary visual cortex (V1), they are involved in whisker-dependent touch (Yu et al., 2019) or visual feature selectivity (Atallah et al., 2012; Lee et al., 2012; Wilson et al., 2012). Previous work has demonstrated that PV cINs receive strong inputs from the thalamus and provide feedforward inhibition (FFI) (Cruikshank et al., 2010; Porter et al., 2001) within the whole cortex, while SST cINs receive reciprocal cortical inputs, allowing them to mediate feedback inhibition (Sil-

berberg and Markram, 2007). However, both the thalamus and cortex are comprised of functionally distinct inputs, which have not been described in these canonical circuits. It is also well accepted that environment plays a critical role in the development of cortical neurons (Chou et al., 2013; De Marco García et al., 2015; Li et al., 2013; Pouchelon et al., 2014; Quattrocolo et al., 2017). For example, the development of PV cIN FFI (Marques-Smith et al., 2016; Tuncdemir et al., 2016), which is thought to contribute to cortical plasticity in visual (Hensch, 2005; van Versendaal and Levelt, 2016) and somatosensory systems (Le Magueresse and Monyer, 2013), has been shown to be regulated by early thalamic activity (Chittajallu and Isaac, 2010; Daw et al., 2007). These studies suggest that the nature of the input may regulate the maturation of cINs in an activity-dependent and areal-specific manner. Recent work, however, has shown that at a genetic level, each of the discrete cIN subtypes is remarkably similar regardless of cortical area (Tasic et al., 2016). This suggests that cIN identity is intrinsically determined prior to settling within the cortex. If so, it seems likely that the afferents they receive are dictated by cell type. This raises the conundrum

of how PV and SST cINs can adapt their function in accordance with the particular sensory, motor, or associative area they occupy.

To explore this question, we undertook a systematic examination of the development of the afferent connectivity to PV and SST cINs in the deep layers of ALM, S1, and V1 using monosynaptic rabies (RV) tracing, complemented by physiological analysis. This revealed that the balance of PV and SST cIN local and long-range afferents are primarily defined by PV and SST cIN areal location. In addition, the number of afferent neurons, as well as the dynamics of how these inputs form during development, varied in PV versus SST cINs. Moreover, both areal- and cell-type-specific connectivity are perturbed by changes in early activity or in a fragile X syndrome model. These data provide a comprehensive map of cIN afferents within different functional cortical areas and reveal the region-specific development by which PV and SST cIN circuits are established.

RESULTS

Mapping developmental changes in the afferent connectivity of PV and SST cINs

To uncover the specificity and development of PV and SST cIN circuits, we compared their presynaptic afferents within ALM, S1, and V1 using rabies (RV) retrograde labeling (Figures 1A and 1B). To limit variability within PV and SST cINs, we focused our analysis on the deeper layers of the cortex, layers 5 and 6 (Figures 1D and S1A), as they are the first to mature. We selected the CVS N2c RV strain (Reardon et al., 2016), as it is less toxic and more comprehensively reports afferent connectivity than the originally used B19 variant (Wickersham et al., 2007). Rabies tracing is achieved by infecting starter cells with an AAV-helper that provides dual complementation allowing for rabies infection (TVA) and monosynaptic transport (G protein) (Figure 1A, left; Figure S1B). Here, we combined both helper elements (TVA and N2cG) and a reporter (eGFP) into a single AAV-helper virus (AAV-DIO-helpers Figure 1A, middle). This was essential for the accurate determination of starter cells and quantification of connectivity.

As somatostatin expression initiates early in development, we used SST-Cre mice to target SST cINs both during development and in adulthood. However, while we could use PV-Cre to target adult PV cINs, the late onset of parvalbumin gene expression prevents its use for developmental time points (up to P20 in V1; Figure S1C). For PV cIN early targeting, we therefore developed a Boolean-based intersectional AAV strategy. Lhx6$^+$ progenitors give rise to both PV and SST cINs and provide an early marker for both populations (Flandin et al., 2011; Mayer et al., 2018; Tyson et al., 2015; Vogt et al., 2014). The coincident early expression of somatostatin with Lhx6 allowed us to implement a subtractive (Lhx6-iCre-ON / SST-FlpO-OFF) strategy for preferentially targeting early PV cIN populations. Lhx6-iCre triggers the expression of DIO helpers, while SST-FlpO abrogates the expression of this virus within the SST population (AAV-IS-helpers; IS: intersectional; Figure 1A middle). While the AAV-helper virus was injected at P0, N2cRV was injected at P5. This was necessary to allow for the suppression of the helper virus within the off-target SST population. To verify the PV targeting specificity, we confirmed that the targeted population was

uniformly SST-negative. Five days post injection, we found high specificity for putative PV cINs (i.e., Lhx6$^+$/SST$^-$). By P15, the age of onset of parvalbumin expression, some SST negative cells had begun to colocalize with parvalbumin (Figure 1C; SST$^-$ 73.67% ± 3.03 in ALM; 73.77% ± 0.84 in S1; 76.60 ± 3.96 in V1 at P5; 93.94% ± 1.53 in ALM; 97.17% ± 1.67 in S1; 94.75 ± 1.96 in V1 at P15. PV$^+$ 23.34% ± 10.88 in ALM; 45.47% ± 16.22 in S1; 13.28% ± 6.06 in V1 N = 3 each), while at P30, the majority colocalized with PV (Figure S1D; PV$^+$ 90.99% ± 3.66 n = 3 in ALM; 84.47% ± 4.78 n = 5 in S1; 74.45% ± 6.57 n = 4 in V1). Starter cells were manually quantified for colocalized helper-GFP and rabies-mCherry$^+$ cells (Figures 1D, 1E, S1A, and S1B; Table S1).

Retrogradely labeled neurons were defined using anatomical atlas alignment and the degree of connectivity from the neurons retrogradely labeled in each brain structure was normalized in accordance with the total number of retrogradely labeled neurons, as previously described (Åhrlund-Richter et al., 2019; Cohen-Kashi Malina et al., 2021; Wall et al., 2016) (Figures 1B and 1E; STAR Methods; N = 21 total adult control animals: N = 11/10 PV/SST cINs; N = 3-4 per cell type within each area and N = 20 total P10 control animals; N = 9/11 PV/SST cINs; n = 3-4 per cell type within each area).

To visualize the global tracing for each population (Figures 1B and 2A) and to confirm the results obtained manually, we developed an automated method for quantifying our results. We created N2c rabies expressing a nuclear tdTomato reporter (H2B:tdTomato, Figure S1F) to aid in this effort, as the reporter improved the software's ability to accurately detect retrogradely labeled cells. Automatic quantification aligned well with the manually obtained numbers (Figure S1E), bolstering our confidence in our results.

Presynaptic inputs to PV and SST cINs are primarily determined by their areal location

Previous studies using RV tracing detected very small differences between the connectivity of cIN subtypes but did not compare their connectivity within different cortical areas (Sun et al., 2019; Wall et al., 2016; Shouhua Zhang et al., 2019; Siyu Zhang et al., 2016). We hypothesized that differences in connectivity rely upon the regional location in which PV and SST cells settle, as previously suggested from medial prefrontal cortex (mPFC) tracing (Åhrlund-Richter et al., 2019). We, therefore, examined PV and SST cIN afferent connectivity across three distinct cortical areas: ALM, S1, and V1 (Figures 1A and 2A). Principal component analysis and unsupervised K-means clustering of all cases (N = 41) revealed that afferents to PV and SST cINs segregate in accordance with the areal location of PV and SST cINs both during adulthood and development (Figure 2B). The strong areal influence on connectivity is confirmed by the high Pearson's correlation coefficient between both cIN populations within each area at both time points (Figure 2C)

To examine the contribution of the specific presynaptic inputs in the areal-specific organization of PV and SST cINs afferent circuits, we performed multiple linear regressions using cell types ("cell"), areal location ("area") and time points ("time") as categorical indicators, followed by an F-test (STAR Methods). For the "area" indicator, the highest F-values of the majority of presynaptic structures, which reveals how much regression model
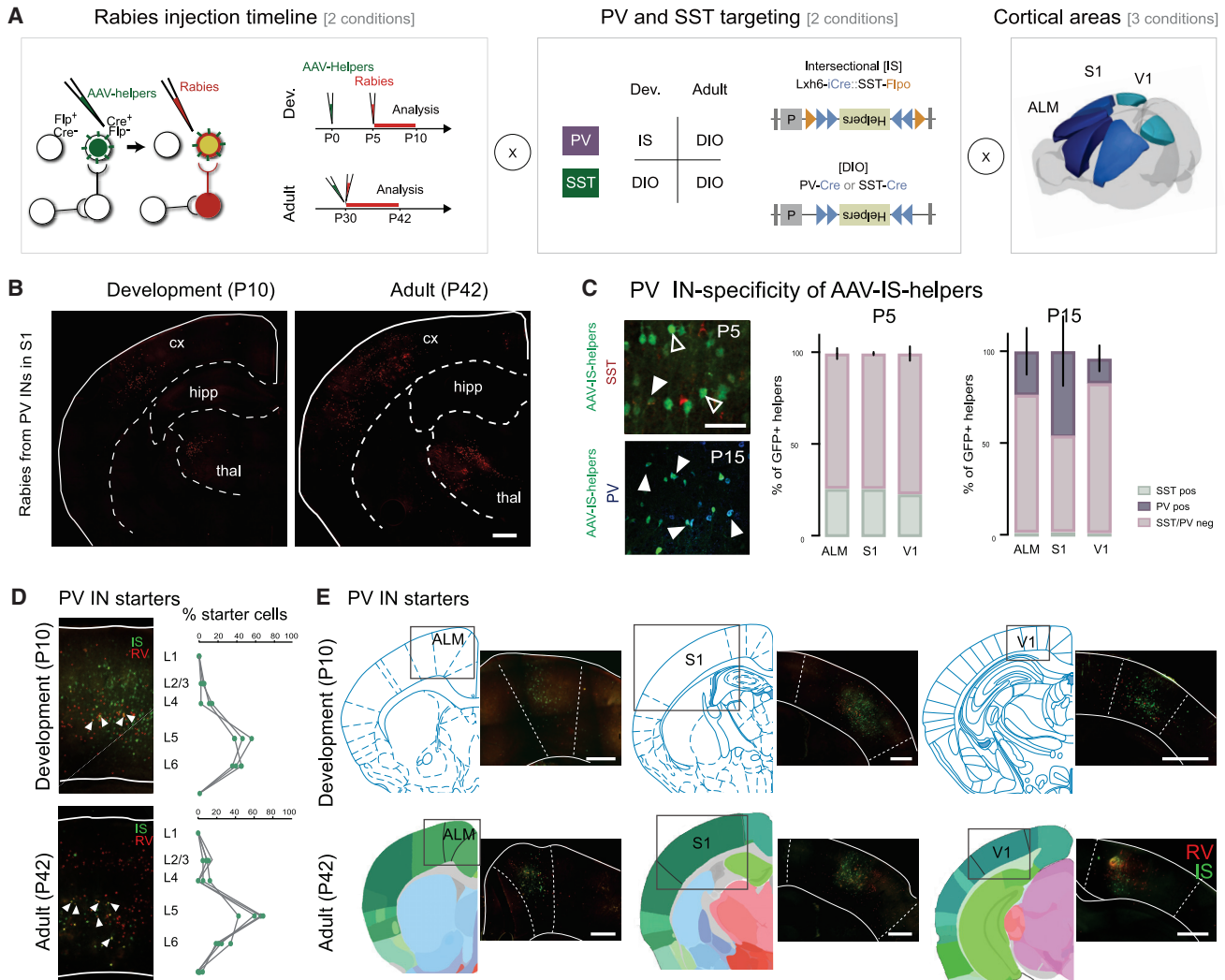
Figure 1. Mapping developmental changes in the afferent connectivity of PV and SST cINs

(A) Experimental design of PV and SST cINs afferent rabies retrograde tracing. Left panel: principle of modified rabies tracing with the timeline of AAV-helpers and N2cRV injections for the developmental time point (top) and for the adult time points (bottom). TVA and N2cG conditional helpers (in green) are expressed using AAVs, followed by the specific infection and retrograde labeling by EnVA-pseudotyped CVS N2c rabies virus (Rabies, in red). Middle panel: PV Cre- and SST-Cre mouse lines are used with AAV-DIO-helpers construct (bottom). Intersectional strategy using Lhx6-iCre/SST-FlpO mouse lines is used with the AAV-IS-helper (top). Right panel: The tracing was performed from both PV and SST cINs populations within 3 cortical areas (ALM, S1 and V1).

(B) Example of retrograde labeling from PV cINs in S1 at a developmental (P5-10) and adult (P30-42) time points (scale bar: 500 μm).

(C) The specificity of the PV cINs targeting using AAV-IS-helpers was verified with somatostatin staining (red) at P5 and P15 and with parvalbumin staining (blue) at P15 (left panel). Percentage of parvalbumin-positive versus somatostatin-negative in AAV-IS-helpers infected population at P5 and P15 in ALM, S1, and V1 (right panel). Data shown are as mean ± SEM.

(D) Examples of starter cells (colocalization of helpers (green) with RV (red). Percentage of starter cells quantified per layer (scale bar: 100 μm). Circles represent individual animals.

(E) Examples of AAV-helpers localization within ALM, S1 and V1 during development, P5-P10, and in adults, P30-P42, together with their corresponding atlas Paxinos at P6 for the development and Allen Institute Brain reference atlas for adults (scale bar: 200 μm). Circles represent individual animals.

for each indicator fits the data better, reached significance (such as cortical inputs, ACA, S1 or thalamic inputs dLG, VB; Figure 2D; see STAR Methods and legends for abbreviations). Interestingly, "cell" is not a predictor of the presynaptic input specificity, while "time" provides some predictive value, but less than "area". Because presynaptic inputs originate from regions known to project to specific areas (such as thalamic dLG nucleus to V1

or VB nucleus to S1), we also investigated analogous inputs across areas, i.e., local cortex (such as V1 or S1) or first-order thalamus (such as dLG, VB; see STAR Methods for the full description). Like for all afferents, analogous afferents to PV and SST cINs are primarily predicted by their areal location ("area"), progressively followed by developmental time points ("time") and then cell types ("cell") (Figure 2E).
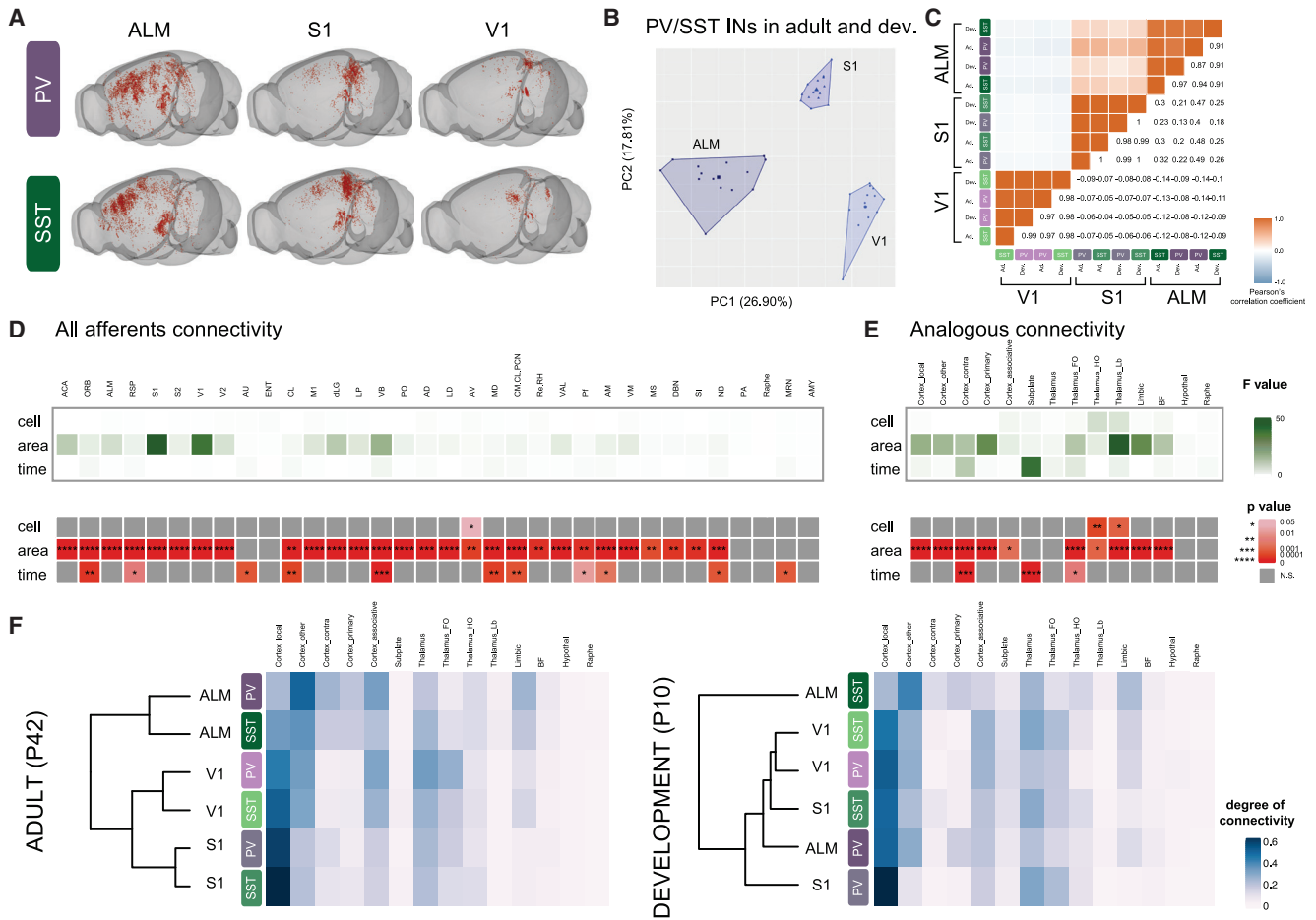
Figure 2. Presynaptic inputs to PV and SST cINs are primarily determined by their areal location

(A) Examples of rabies retrograde labeling from PV and SST cINs in ALM, S1, and V1 using "Brainrender" 3D representation (Claudi et al., 2020).

(B) Principal component analysis (PCA) of using degree of connectivity for all afferents I each animal (N = 21), showing the clustering, using K-mean analysis, of both PV and SST cINs, both during development and adulthood into 3 areal-specific clusters (ALM, S1 and V1).

(C) Correlation plot of pearson's correlation coefficients based on the degree of connectivity of all N shows the high correlation between PV and SST cINs both during development and adulthood within each area.

(D) Heatmap of the F values (top) and the p values (p, bottom) calculated after multiple linear regression using "cell" (PV versus SST cINs), "area" (ALM versus S1 versus V1), and "time" (development versus adult) as categorical indicators. Only significant p are represented, with *p < 0.05, **p < 0.01, ***p < 0.001, ****p < 0.001. See abbreviations of the origin of the afferents below.

(E) Same as (D), but using afferents grouped in analogous types instead. See STAR Methods for the groups.

(F) Heatmap and hierarchical clustering of PV and SST cINs in ALM, V1, and S1 using the degree of connectivity from analogous afferents in adults (left) and during development (right).

Abbreviations: Cortex: primary and secondary motor (M1, ALM) visual (V1, V2), somatosensory (S1, S2), auditory (AU), retrosplenial (RSP), cingulate (ACA), orbital (ORB), entorhinal (ENT), claustrum (CL) areas, amygdala (AMY); Thalamus: laterodorsal (LD). Lateroposterior (LP), dorsal lateral geniculate (dLG), posterior (PO), ventrobasal (VB), ventral anterior and lateral (VAL), anteromedial (AM), anteroventral (AV), centromedian, central lateral and paracentral (CM/CL/PCN), medi-odorsal (MD), Reuniens and Rhomboid (Re/RH), anterodorsal (AD), Parafascicular (Pf) nuclei; basal forebrain: medial septum (MS), substantia innominate (SI), diagonal band nucleus (DBN), nucleus basalis (NB); hypothalamus: preoptic area (PA); hindbrain: raphe nucleus (Raphe), middle reticular nucleus (MRN).

Next, we used hierarchical clustering to investigate the interaction of cell-type versus areal specificity of the analogous afferents during development compared to adulthood. Remarkably, adult PV and SST cINs cluster by area (Figure 2F, left), as previously observed for unsupervised clustering of all afferents. During development, however, the areal-specific distribution is not yet apparent (Figure 2F, right). Only PV and SST cINs in V1 group together, while SST cINs in ALM form their own group. V1 is the least mature cortical area at P10 (Bayer and Altman, 1987; Fox and Wong, 2005) and our physiological analysis indicates that SST cINs in ALM are the most mature (Figures S3B and S3D), suggesting that the afferent developmental dynamics reflect the maturation of PV and SST cINs according to the region in which they are imbedded, and that areal-environment regulates the development of cIN presynaptic circuits during postnatal development.
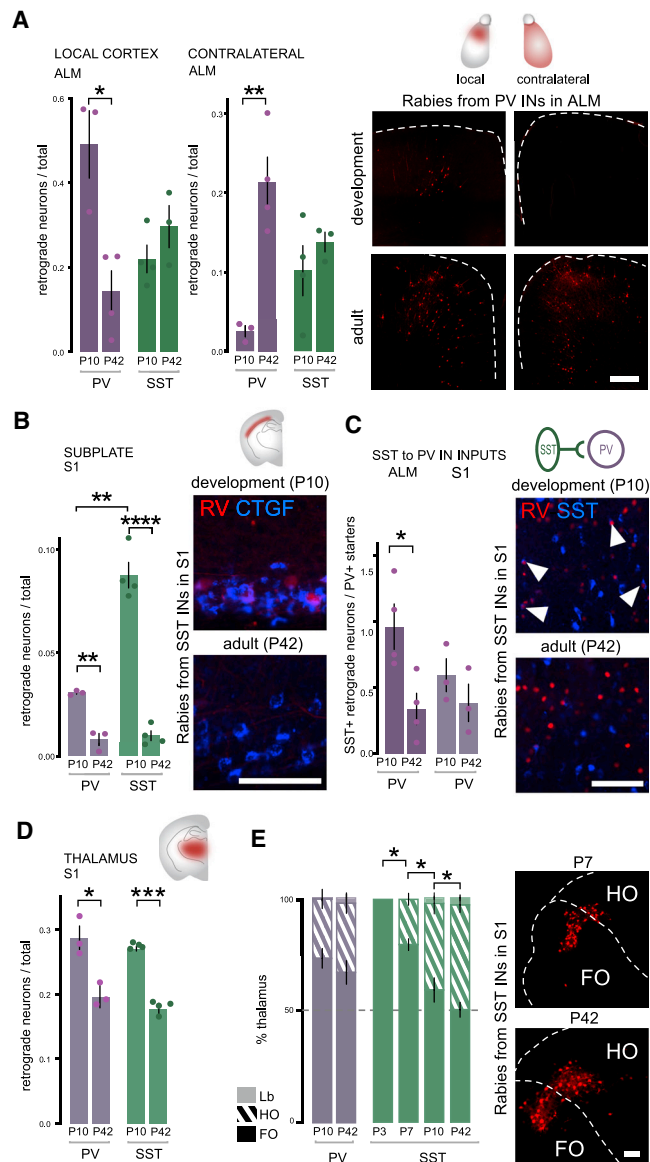
Figure 3. During development, areal-specific presynaptic inputs onto cINs are dynamically regulated in a cell-type-specific fashion

(A) Early establishing connectivity within local cortex and late-establishing connectivity of contralateral cortex from PV and SST cINs within ALM during development (P5-P10) and in adults (P30-P42). Quantification: Local cortex: PV cINs development comparison Student's t test *p = 0.0111, SST cINS comparison is non-significant (n.s.). Contralateral: PV cINs development comparison Student's t test **p = 0.0046. SST cINs n.s. Examples of RV retrograde tracing from PV cINs in ALM and in the contralateral side (scale bar: 200 μm).

(B) Early establishing connectivity of subplate neurons is higher on both PV and SST cINs during development in S1. Student's t test PV cINs **p = 0.0016; SST cINs ****p < 0.0001. However, subplate connectivity is higher onto SST than PV cINs at P10. Student's t test ***p = 0.0006. Example of rabies-labeled neurons (red) colocalization with CTGF maker (blue) in L6b (scale bar: 50 μm).

(C) Early SST cIN transient connectivity to PV cINs. PV cINs Student's t test *p = 0.0247 in ALM, n.s. in S1. SST cINs are identified as local RV+ neurons (RV) colocalizing with somatostatin (SST, bue) and normalized with the number of PV starter cells (see Figure 1, colocalization of RV+ and helpers-GFP) (scale bar: 50 μm)

During development, areal-specific presynaptic inputs onto cINs are dynamically regulated in a cell-type-specific fashion

Our regression analyses revealed that developmental time course and cIN types provide predictors of presynaptic connectivity in addition to areal specificity. Therefore, we examined the temporal dynamics by which individual areal inputs are established onto PV and SST cINs. More specifically, we examined the temporal dynamics of afferents from cortical and thalamic subtypes in order to compare how they align with their previously described canonical connectivity. Two trends emerged. First, in a majority of cases, we observed a progressive increase in connectivity throughout development with a late maturation of the presynaptic inputs. Second, presynaptic inputs were established early in development, and either were maintained or regressed as development proceeded. Notably, even in cases where precocious connectivity occurred early in development, such projections were eclipsed by the arrival of later afferents, resulting in these early projections becoming a minority by adulthood (Figures 3 and S2). For example, the substantial contralateral connectivity seen onto adult PV cINs in ALM is a result of progressive maturation, which while minimal at P10, is much higher onto PV compared to SST cINs at P42 (Figure 3A right). In contrast, local connectivity to PV cINs in the ALM is an example of early maturation where connectivity is already established by P10 (Figure 3A left). Notably, both contralateral and local connectivity to SST cINs remain constant during development.

A subset of early connectivity has been previously described as transient (Kanold and Shatz, 2006; Marques-Smith et al., 2016; Tuncdemir et al., 2016). Among these were subplate neurons, identified based on their deep location in layer 6b of the cortex and a portion of which were confirmed with CTGF+ staining (Hoerder-Suabedissen et al., 2009). In S1, the dynamics of subplate connectivity to SST and PV cINs was particularly striking. At P10, SST cINs in S1 have considerably higher afferent connectivity from the subplate than PV cINs. Although not completely absent, the mature connectivity onto both PV and SST cINs is low in adults (Figures 3B and S2C). Another type of transient connectivity was seen in the developmental connectivity between SST to PV cINs. Previously described as having stronger early connectivity (Marques-Smith et al., 2016; Tuncdemir et al., 2016), somatostatin positive cINs in all three cortical regions were labeled by local RV tracing from PV cINs during development (Figure 3C and S2B). Notably, at P10 the SST cIN connectivity to PV cINs was particularly marked in ALM

(D) Early connectivity from the thalamus in S1. PV cINs Student's t test *p = 0.0218, SST cINs Student's t test ****p < 0.0001.

(E) Ratio of FO, HO, and Lb neurons (see STAR Methods for definition of the classes) within whole thalamic afferent populations (100%). PV cINs receive a higher proportion of FO afferents at both time points in S1, while SST receive a similar amount of FO and HO afferents at P42. The proportion of FO to SST cINs gradually lowers during development. One-way ANOVA followed by Tukey's test adjusted p values: P3/P7 *p = 0.0118; P7/P10 *p = 0.0222; P10/P42 *p = 0.0236. Examples of FO/HO proportion from the retrograde RV labeling from SST cINs in S1 during development (at P7) and in adult (scale bar: 100 μm).

Data shown are as mean ± sem. Circles represent individual animals.

(Figure 3C). Moreover, we found that SST to PV cIN connectivity remained present in ALM, S1, and V1 in adulthood, although equivalently reduced in number (Figure S2B).

We next investigated the afferent thalamic projections to PV versus SST cINs during development. Thalamocortical (TC) connectivity during development has mostly been studied in sensory systems. However, we find that the thalamus is equivalently connected to cINs in ALM relative to either S1 or V1 (Figure S2F). In adult primary sensory areas, TC projections are known to be stronger to PV compared to SST cINs. In particular, PV cINs have been shown to provide FFI to pyramidal neurons (Cruikshank et al., 2010; Tan et al., 2008). However, as a general rule, we found that the thalamic neuron projections to PV and SST cINs are both equivalent in number and established early (Figure 3D; Tukey's test P10 versus P42 PV p value (p) = 0.0218; SST p < 0.0001). Nonetheless, we did observe that specifically in S1, distinct thalamic neuronal subtypes differentially innervate these populations.

Within the thalamus, neurons are hierarchically organized within nuclei in accordance with their cortical connectivity. Thalamic afferents emanating from particular nuclei serve different functions (Shepherd and Yamawaki, 2021; Williams and Holtmaat, 2018; Yu et al., 2019). Therefore, we examined TC projections to cINs originating from the three hierarchical classes of thalamic nuclei: first order (FO), higher order (HO) and limbic (Lb) (Figures S2D and S2E; STAR Methods) (Diamond et al., 2008; Frangeul et al., 2016; Phillips et al., 2019). We found that TC connectivity onto PV and SST cINs depended upon their areal location. Specifically, within S1 (see Figure S2G for V1 and ALM), while PV cINs receive more FO than HO inputs, SST cINs receive a similar amount from both classes, although the FO afferents arrive earlier (Figure 3E; in adult PV FO: 66.93% ± 5.22, HO: 30.84% ± 4.50, Lb 2.23% ± 1.68; SST FO: 50.13% ± 3.25, HO: 46.73% ± 3.33, Lb: 3.14% ± 1.25). As a result, both PV and SST cINs receive more FO afferents at P10 (at P10; PV FO: 73.10% ± 4.33, HO: 26.43% ± 4.24, Lb 0.40% ± 0.12; SST FO: % 58.928 ± 5.38, HO: 38.65% ± 4.67, Lb: 2.42% ± 0.80). Although we are presently unable to examine the earlier connectivity of PV cINs, the early expression of somatostatin, coupled with our DIO targeting strategy, allowed us to investigate the TC connectivity of SST cINs from birth. Remarkably, during early postnatal periods, SST cINs receive only FO thalamic afferents (SST P0 FO 100% ± 0; P3: FO:79.66% ± 2.64. ANOVA followed by Tukey's test P3-P7 p = 0.0118; P7-P10 p = 0.0222; P10-P42 p = 0.0236). Finally, to a considerably lesser extent, both PV and SST cINs receive TC limbic afferents. ALM receives proportionately more limbic input than either S1 or V1 (Figure S2G), which is consistent with its role in decision making (Li et al., 2015; Wu et al., 2020).

Taken together, the developmental dynamics by which mature circuits of PV and SST cINs are achieved are markedly different across regions.

The timing of PV and SST cIN physiological maturation varies across cortical areas

FFI mediated by PV cINs only develops after P8-P12 (Chittajallu and Isaac, 2010; Murata and Colonnese, 2016) in S1 and V1, suggesting that the temporal dynamics of afferent development

is tightly coupled with cIN maturation. However, no study to date has systematically investigated the areal maturation of cINs. We therefore next investigated whether the timing of when PV and SST cINs receive afferent projections corresponds with their maturation across cortical regions.

To investigate whether areal environment is a factor for the maturation trajectory of PV and SST cINs, we examined the intrinsic properties of PV and SST cINs at P10 compared to P40 in ALM, S1 and V1 (Table S2; Figure 4A). We used an equivalent intersectional strategy to that used for the RV tracing. Lhx6-iCre::SST-FlpO animals were crossed with an intersectional reporter (IS reporter) (He et al., 2016), resulting in the labeling of putative PV cells with tdTomato, while SST FlpO transforms this allele to a GFP reporter (Figure S3A). To examine their whole physiological properties, we patched the labeled populations within the deeper layers of the cortex. As previously described (Tuncdemir et al., 2016), both PV and SST cINs look immature at P10 (Figures 4B, S3B, and S3C). However, the characteristics specific to PV and SST cINs (e.g., spiking frequency, adaptation, spike threshold; Table S2; ALM PV n = 7, SST n = 8, S1 PV n = 10, SST n = 12, V1 PV n = 15, SST n = 15), vary across both development and area. We selected the three most significant properties for PV and SST cINs specification at P10 and P40, respectively (Figure S3D), and plotted the cells in accordance with these parameters. cIN subtypes are intermixed during development, but cluster into defined populations in adulthood. At P10, ALM shows better segregation than S1, while in V1 these populations completely overlap (Figure 4C). Hence, the unique mature physiological properties, which define PV and SST cINs, appear in an areal-specific manner.

Development of cIN afferent connectivity is disrupted in fragile X syndrome disorder or upon early sensory experience defects

Since temporal dynamics of afferent development predict the maturation of PV and SST cINs, we investigated whether developmental perturbations to cortical environment affect the establishment of normal afferent connectivity. We examined two types of perturbation: (1) early visual or somatosensory activity disruption, and (2) a genetic model of the developmental disorder fragile X syndrome.

PV cIN connectivity, and more specifically their thalamocortical inputs, have been shown to be dynamically regulated during the postnatal stages, when early sensory activity is essential to shape circuitry in visual (Ackman et al., 2012; Burbridge et al., 2014) and somatosensory areas (Pouchelon et al., 2014; Tuncdemir et al., 2016). We therefore tested whether early sensory experience influences the development of presynaptic inputs onto PV and SST cINs. We performed either infraorbital nerve section (IONS) or enucleation (Enuc) at P0 to disrupt whisker-dependent and visual inputs respectively. Using RV tracing, we then examined the afferents to these cIN populations at mature time points after the closure of their respective sensory critical periods (P30-42 for S1 and P40-52 for V1; Figure 5A). In addition, previous examination of autism models showing area-specific disruptions suggests that areal connectivity may also depend on genetic determinants (Parikshak et al., 2016). Therefore, we examined the presynaptic connectivity of PV and SST cINs in
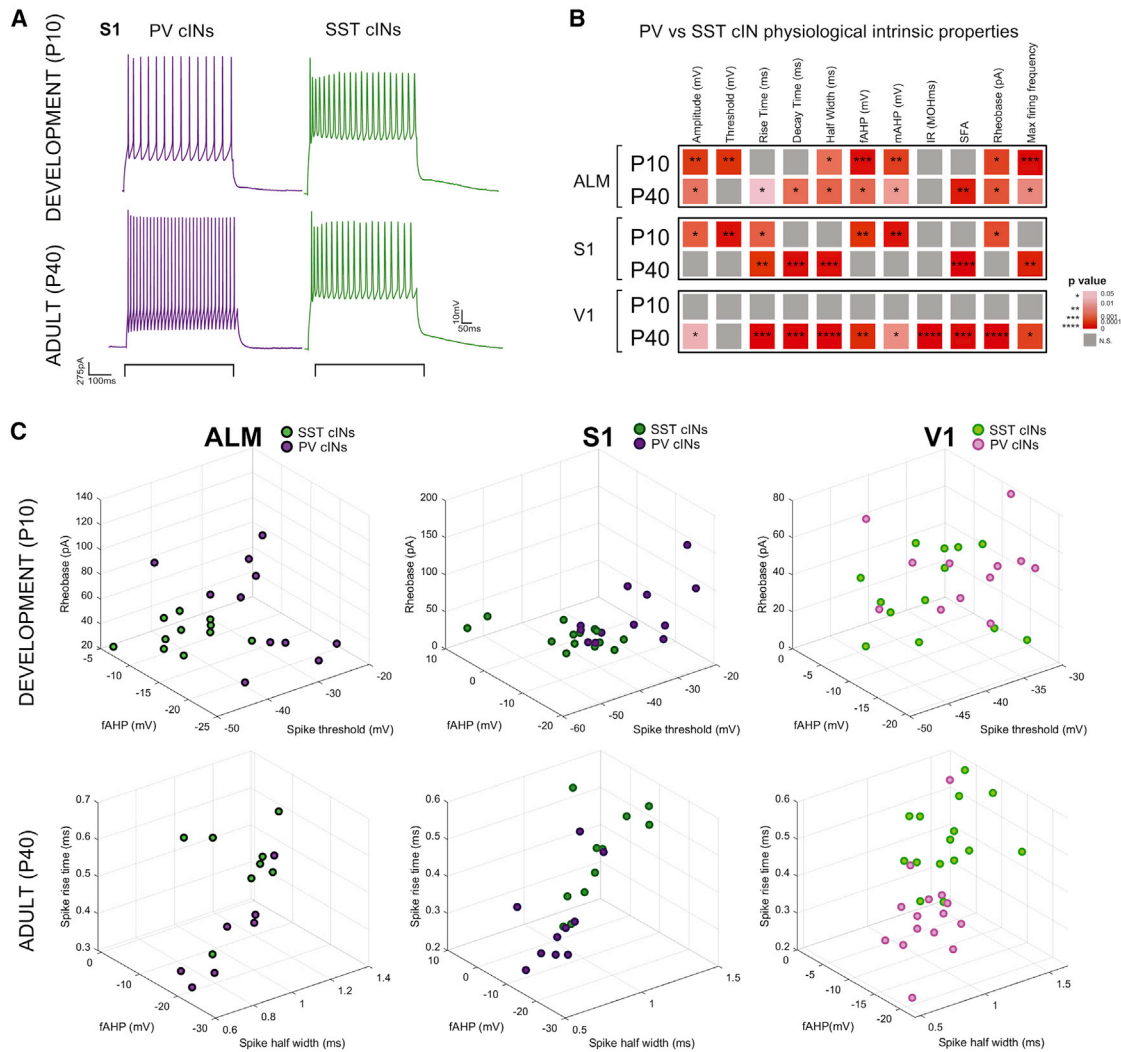
Figure 4. The timing of PV and SST cIN physiological maturation varies across cortical areas

(A) Example of electrophysiological trace of patch clamp recording from PV and SST cINs in S1 at P10 and P40, showing their maturation.

(B) Heatmap of p values from Sidák's multiple comparison test between PV and SST cINs average features within each area at P10 and P40. *p < 0.05, **p < 0.01, ***p < 0.001, ****p < 0.00001. Grey is n.s. More physiological properties or more significance was detected at P40 between PV and cINs reflecting their maturation. See below for abbreviations of the features.

(C) 3D plot of all PV and SST cINs within ALM, S1 and V1 during development and in adults using the most significant features at P10 and P40. Clustering of PV and SST populations are more evident at P40 and the least in V1 at P10.

Abbreviations: fAHP, mAHP = fast-, medium-afterhyperpolarization; IR = input resistance; SFA = spike frequency adaptation.

the S1 cortex of a fragile X syndrome model, using male KOs for *Fmr1* (Dutch-Belgian Fragile X Consortium, 1994). The 3 models and their respective controls (from Figures 2 and 3) were then examined for alterations in their presynaptic afferents (Fold changes and p values in heatmaps, compared to their corresponding controls: Ctrl SST S1 N = 5; Ctrl PV S1 N = 3; SST IONS N = 3; PV IONS N = 4; Ctrl SST V1 N = 3; Ctrl PV V1 N = 4; SST Enucleation N = 3; PV Enucleation N = 3; SST Fmr1 KO N = 5; PV Fmr1 KO N = 4). Interestingly, cIN cell types in each experimental condition showed unique patterns of afferent connectivity disruption (Figures 5B and S4). When afferents were affected by any of the three perturbations, the trend was consis-

tently in the same direction. For example, in both Fmr1 KOs and IONS animals, SST cINs thalamic afferents were increased while cholinergic afferents to PV cINs were decreased (Figure 5B).

Because either the whole thalamus (Figure S4B) or at least one of the hierarchical thalamic groups was perturbed in each experimental condition, we examined the relative proportion of hierarchical thalamocortical classes disrupted in sensory deprived and Fmr1 KO animals (Figures 5C and S4C). We found that despite a global increase of thalamocortical afferents, the normal ratio of FO to HO afferents was not disrupted on SST cINs in whisker-deprived animals (IONS). By contrast, in Fmr1 KOs there was a relative increase in the percentage of FO afferent neurons and

Figure 5. Development of cIN afferent connectivity is disrupted in fragile X syndrome disorder or upon early sensory experience defects

(A) Experimental timeline: visual or somatosensory deprivation at P0 (Enuc = enucleation (eye removal) and IONS = infraorbital nerve section for whisker deprivation, respectively), followed by N2cRV+AAV-helpers injection in PV-Cre and SST-Cre animals, at P40 or P30 and in V1 or S1, respectively. Fmr1 KO males crossed with PV-Cre or SST-Cre were used for N2cRV+AAV-helper injections at P30 in S1.

(B) Heatmap of log2(fold change) and the p values from the difference between average analogous connectivity between Enuc, IONS or Fmr1 KO animals and their respective controls (PV and SST cIN WT from S1 or V1 from Figures 2 and 3) tested with Student's t test *p < 0.05, **p < 0.01, ***p < 0.001, ****p < 0.00001. Grey boxes are n.s.

(C) Ratio of FO, HO and Lb thalamic neurons within the whole thalamus (100%). SST cIN TC afferent proportion is changed only in the Fmr1 KOs (One-way ANOVA followed by Tukey's test (adjusted p values): %FO p = 0.018; for %HO p = 0.043, for %Lb p = 0.026); PV cIN TC afferent proportion is disrupted in both IONS and Fmr1 KO animals (One-way ANOVA, Tukey's test: %FO IONS **p = 0.0063; Enuc *p = 0.039). Examples of FO/HO distribution from S1 PV cIN RV tracing (Scale bar: 100 μm).

a near complete loss of Lb neurons (ANOVA test followed by the post hoc Tukey multiple comparison test: Ctrl versus IONS non-significant (n.s.); Ctrl versus Fmr1 KO adjusted *p* for %FO p = 0.018; for %HO p = 0.043, for %Lb p = 0.026). On the other hand, under no conditions examined was the net amount of thalamic afferent connectivity onto PV cINs affected (Figures 5B and S4B). However, there was a consistently observed relative decrease in the percentage of FO afferents (Figures 5C and S4; ANOVA, Tukey test: Ctrl versus IONS for %FO p = 0.006; for %HO p = 0.005; for %Lb p = n.s.; Ctrl versus Fmr1 KO for %FO p = 0.039; for %HO p = 0.034; for %Lb p = n.s.).

In summary, both PV and SST cIN afferent connectivity is influenced by changes in early sensory activity and by genetic mutation.

DISCUSSION

Here we addressed the paradox that, despite considerable functional differences between regions, specific types of cINs are genetically similar (Tasic et al., 2018) and are thought to form canonical circuits. In this study, we find that both PV and SST cINs receive similar inputs within given areal territories, indicating that the afferent connectivity of these cells is influenced by the region in which they are embedded. However, across development, the order in which cIN types receive afferents is reflective of both their cell type identity, as well as the region in which they are found. Specifically, both PV and SST cINs within particular regions receive afferents in a predictable order, which varies dependent on the areal region considered. This indicates that

a combination of intrinsic subtype identity and nonautonomous areal-specific cues result in a unique pattern of afferentation occurring within specific areas. Nonetheless, the fact that both cell types within particular cortical areas ultimately receive a similar balance of afferents indicates cINs adapt their connectivity in accordance with their settling positions. This reveals the logic by which areal-specific cues guide the formation of canonical cIN circuits.

Since the maturation of cIN physiological properties correlates with their formation of afferent connectivity, it is interesting to speculate whether this relationship is causal. In part, our examination of sensory deprivation and the fragile X syndrome model provides clues to the required underlying signals. In the future it will be intriguing to examine whether these perturbations impact the timing at which mature physiological properties emerge. Conversely, as the mature intrinsic properties are reflective of cell type, the causal relationship may be that the intrinsic maturation of PV and SST cINs determines the timing at which they are competent to receive particular afferents. In sum, this work indicates that the formation of cIN circuits results from a unique combination of autonomous and non-autonomous signals. We suggest that some originate from the cINs themselves, while others are communicated from the adjacent excitatory cell types, as well as from the long-range afferents that impinge upon them.

Intrinsic properties, and therefore the functions of PV and SST cINs, are diverse and can be classified into subtypes (at least for SST cINs). Therefore, it would be of interest to relate the emergence of intrinsic physiological traits of distinct subtypes of

SST cINs to the development of their afferents. SST cIN subtypes are primarily arranged according to the cortical layers of the cortex. More specifically, in the deeper layers of S1, which we target here, SST cINs are comprised by ~60% of Martinotti cells (10% T-shaped, 50% Fanning-out) and ~40% of non-Martinotti cells in S1 (Nigro et al., 2018). Connectivity in distinct areas could originate from distinct proportions of cIN subpopulations if each subtype receives distinct afferentation. Such results would demonstrate a strong role for cell-autonomous signals into the afferent development of SST cINs.

Indeed, recent work suggests that cINs are evolutionarily more conserved than neocortical pyramidal cells (Tosches et al., 2018), suggesting a strong intrinsic genetic contribution to cIN development. This is consistent with the notion that there is a tight coupling between presynaptic input and postsynaptic identity of cINs. The restricted genetic plasticity of cINs during circuit formation by constraining connectivity provides a degree of stability that may ensure proper cortical wiring. Nonetheless, we do observe that afferent TC connectivity to PV cINs is regulated by sensory activity. It has long been shown that sensory activity dictates the critical period of plasticity during development (Antón-Bolaños et al., 2018; Erzurumlu and Gaspar, 2012; Hensch, 2005), in particular through TC-FFI (Chattopadhyaya et al., 2004; Chittajallu and Isaac, 2010; Maffei et al., 2006; Miska et al., 2018) and perisomal inhibition provided by PV cINs (Espinosa and Stryker, 2012; Kuhlman et al., 2013; Southwell et al., 2010). Here we show that within PV cINs, sensory activity regulates their receipt of FO versus HO afferents. FO projections solely carry sensory information, while HO projections are thought to actively integrate sensory-motor signals and thus regulate contextual or attention-related behaviors (Erzurumlu and Gaspar, 2012; Roth et al., 2016; Saalmann et al., 2012). Our results indicate that within PV cINs, FO-driven FFI drives experience-dependent plasticity, and conversely, we speculate that HO inputs attenuate it. Consistent with this hypothesis, PV cINs in ALM, an area involved in motor-planning and attention, are primarily driven by HO inputs and have not been shown to undergo critical period plasticity.

Moreover, somatosensory and visual systems have distinct critical periods of development. Interestingly, the impact of sensory deprivations in S1 and V1 do not fully overlap, and cINs display distinct disruptions in their afferent connectivity dependent on the system targeted. This implicates a specific role for environment, as transmitted by specific thalamocortical inputs, in the formation of afferentation.

Fragile X syndrome is known to result from a genetic mutation of *Fmr1*, but the variations in phenotypes observed in patients highlight the associated environmental effects. Here, we show that Fmr1 KOs display multiple afferent defects that combine some of those seen in sensory deprivation (S1 IONS) and other perturbations, underlining the differential effects on circuits resulting from environment versus genetics perturbations, respectively. In addition, since sensory activity is distinct between V1, S1, and most strikingly, ALM, we could expect that different connectivity disruptions in distinct areas highlight the distinct behavioral defects of Fmr1 KO mice. In addition, the observation of both genetic and activity-dependent defects in Fmr1 KOs suggests that early sensory experience may also be perturbed in autism.

Additionally, we confirmed our previous observation that SST cINs transiently project to PV cINs in S1. This connectivity has been shown to be necessary for the development of FFI (Marques-Smith et al., 2016; Tuncdemir et al., 2016) and we now demonstrate that it occurs within multiple areal regions. Moreover, we extend our previous findings by showing that this involves a differential decrease in SST to PV cIN connectivity, depending on the areal territory examined. Specifically within the ALM, SST cINs form larger transitory afferents to PV cINs than in S1 and V1. Interestingly, in adults, both cINs subtypes are dominated by HO TC afferents, consistent with previous work indicating that FFI in mPFC also involves HO projections (MD) onto PV cINs (Delevich et al., 2015). This suggests a potential role for transient SST to PV cIN connectivity in controlling HO-related FFI in associative areas. An additional element that potentially contributes to the formation of TC-cIN circuits is the subplate. The subplate (Kanold and Luhmann, 2010) is a transient developmental structure that has been shown to control the maturation of GABA receptors (Kanold et al., 2003) and the development of TC projections within the cortical plate (Ghosh and Shatz, 1993). We observed that the timing of regression of subplate inputs onto PV and SST cINs is also both cell type and area specific. This suggests a potential role for the subplate in differentially regulating TC connectivity to PV and SST cINs within distinct areas.

In conclusion, our results emphasize the necessity of understanding circuit components with respect to their organization within specific functional areas. We also demonstrate that the timing of afferent connectivity of subtypes is important to how afferent circuitry is established within different areal territories. Our results indicate that while common cIN subtypes are embedded across the cortex, areal and subtype differences in their connectivity exist. As a consequence, conserved cIN subtypes are able to perform specialized functions across distributed cortical networks.

LIMITATIONS OF THE STUDY

To compare areal, cell-type, and developmental connectivity, we measured the degree of connectivity as the number of retrogradely labeled neurons in each brain structure normalized to the total number of retrogradely labeled neurons in each brain as previously reported (Ährlund-Richter et al., 2019; Cohen-Kashi Malina et al., 2021; Wall et al., 2016). This allows the aggregate changes across regions to be reflected in a single measure, reflecting the dynamic alterations in connectivity across development. We chose not to systematically show the input magnitude (labeled neurons normalized to the number of starter cells) for clarity, as this measure is primarily relevant when there are regressive events, which only occur in rare cases. However, in the future, this work would benefit from further physiological study of the dynamics of long-range input formation to correlate anatomical connectivity to strength.

Similarly, future studies could build on the correlation between intrinsic physiological properties of PV and SST cINs and their areal-specific connectivity establishment, to further investigate the longitudinal events within each of the area. While we find that connectivity undergoes a dramatic reorganization between

the first postnatal week and mature stages, the mice in our study are still in adolescence (P30) and therefore could show more changes by the time they reach full adulthood. Taken together, further longitudinal studies are warranted.

Our study provides a large-scale connectivity survey of the fragile X syndrome model. Comparing the results with the extensively described sensory deprivation models supports the disambiguation of cIN genetic identity versus sensory environmental factors involved in the disorder. While this interpretation is speculation at this stage, we hope that our large-scale analyses will be the basis for further investigations. These we expect will be aimed at determining whether connectivity disruptions occur in other forms of autism and whether the etiology of this disease can be associated directly with such putative disruptions.

STAR★METHODS

Detailed methods are provided in the online version of this paper and include the following:

- KEY RESOURCES TABLE
- RESOURCE AVAILABILITY
  - Lead contact
  - Materials availability
  - Data and code availability
- EXPERIMENTAL MODEL AND SUBJECT DETAILS
  - Mice
- METHOD DETAILS
  - Sensory deprivations
  - Histology
  - Rabies tracing
  - Viruses
  - All and analogous afferent description
  - Imaging and data analysis
  - *In vitro* electrophysiology
- QUANTIFICATION AND STATISTICAL ANALYSIS

SUPPLEMENTAL INFORMATION

Supplemental information can be found online at https://doi.org/10.1016/j.celrep.2021.109993.

ACKNOWLEDGMENTS

AUTHOR CONTRIBUTIONS

G.P. and G.F. conceived the project and wrote the manuscript. G.P. and C.K.A., carried out injection experiments. Y.Q., S.K., and G.P. processed brains for quantification. D.D. performed and analyzed physiological intrinsic properties. Y.B. designed and performed the automated analysis with the help of G.P. G.P. and A.M.C.M. manually quantified connectivity. R.C. contributed to the design of automated analysis. E.F. contributed to the design of

rabies injection. K.D.R. provided guidance on N2cRV and AAV use as well as produced nuclear-tdtomato N2cRV.

DECLARATION OF INTERESTS

INCLUSION AND DIVERSITY

REFERENCES

Ackman, J.B., Burbridge, T.J., and Crair, M.C. (2012). Retinal waves coordinate patterned activity throughout the developing visual system. Nature *490*, 219–225. https://doi.org/10.1038/nature11529.

Ährlund-Richter, S., Xuan, Y., van Lunteren, J.A., Kim, H., Ortiz, C., Pollak Dorocic, I., Meletis, K., and Carlén, M. (2019). A whole-brain atlas of monosynaptic input targeting four different cell types in the medial prefrontal cortex of the mouse. Nat. Neurosci. *22*, 657–668. https://doi.org/10.1038/s41593-019-0354-y.

Allen, W.E., Kauvar, I.V., Chen, M.Z., Richman, E.B., Yang, S.J., Chan, K., Gradinaru, V., Deverman, B.E., Luo, L., and Deisseroth, K. (2017). Global Representations of Goal-Directed Behavior in Distinct Cell Types of Mouse Neocortex. Neuron *94*, 891–907.e6. https://doi.org/10.1016/j.neuron.2017.04.017.

Antón-Bolaños, N., Espinosa, A., and López-Bendito, G. (2018). Developmental interactions between thalamus and cortex: a true love reciprocal story. Curr. Opin. Neurobiol. *52*, 33–41. https://doi.org/10.1016/j.conb.2018.04.018.

Atallah, B.V., Bruns, W., Carandini, M., and Scanziani, M. (2012). Parvalbumin-expressing interneurons linearly transform cortical responses to visual stimuli. Neuron *73*, 159–170. https://doi.org/10.1016/j.neuron.2011.12.013.

Avants, B.B., Tustison, N.J., Stauffer, M., Song, G., Wu, B., and Gee, J.C. (2014). The Insight ToolKit image registration framework. Front. Neuroinform. *8*, 44. https://doi.org/10.3389/fninf.2014.00044.

Bayer, S.A., and Altman, J. (1987). Directions in neurogenetic gradients and patterns of anatomical connections in the telencephalon. Prog. Neurobiol. *29*, 57–106.

Burbridge, T.J., Xu, H.-P., Ackman, J.B., Ge, X., Zhang, Y., Ye, M.-J., Zhou, Z.J., Xu, J., Contractor, A., and Crair, M.C. (2014). Visual circuit development requires patterned activity mediated by retinal acetylcholine receptors. Neuron *84*, 1049–1064. https://doi.org/10.1016/j.neuron.2014.10.051.

Chattopadhyaya, B., Di Cristo, G., Higashiyama, H., Knott, G.W., Kuhlman, S.J., Welker, E., and Huang, Z.J. (2004). Experience and activity-dependent maturation of perisomatic GABAergic innervation in primary visual cortex during a postnatal critical period. J. Neurosci. *24*, 9598–9611. https://doi.org/10.1523/JNEUROSCI.1851-04.2004.

Chittajallu, R., and Isaac, J.T.R. (2010). Emergence of cortical inhibition by coordinated sensory-driven plasticity at distinct synaptic loci. Nat. Neurosci. *13*, 1240–1248. https://doi.org/10.1038/nn.2639.

Chou, S.-J., Babot, Z., Leingärtner, A., Studer, M., Nakagawa, Y., and O'Leary, D.D.M. (2013). Geniculocortical input drives genetic distinctions between primary and higher-order visual areas. Science *340*, 1239–1242. https://doi.org/10.1126/science.1232806.

Claudi, F., Tyson, A.L., and Branco, T. (2020). Brainrender. A python based software for visualisation of neuroanatomical and morphological data 179, 268–6. https://doi.org/10.1101/2020.02.23.961748.

Cohen-Kashi Malina, K., Tsivourakis, E., Kushinsky, D., Apelblat, D., Shtiglitz, S., Zohar, E., Sokoletsky, M., Tasaka, G.-I., Mizrahi, A., Lampl, I., and Spiegel, I. (2021). NDNF interneurons in layer 1 gain-modulate whole cortical columns according to an animal's behavioral state. Neuron 109, 2150–2164.e5. https://doi.org/10.1016/j.neuron.2021.05.001.

Cruikshank, S.J., Urabe, H., Nurmikko, A.V., and Connors, B.W. (2010). Pathway-specific feedforward circuits between thalamus and neocortex revealed by selective optical stimulation of axons. Neuron 65, 230–245. https://doi.org/10.1016/j.neuron.2009.12.025.

Daw, M.I., Ashby, M.C., and Isaac, J.T.R. (2007). Coordinated developmental recruitment of latent fast spiking interneurons in layer IV barrel cortex. Nat. Neurosci. 10, 453–461. https://doi.org/10.1038/nn1866.

De Marco García, N.V., Priya, R., Tuncdemir, S.N., Fishell, G., and Karayannis, T. (2015). Sensory inputs control the integration of neurogliaform interneurons into cortical circuits. Nat. Neurosci. 18, 393–401. https://doi.org/10.1038/nn.3946.

Delevich, K., Tucciarone, J., Huang, Z.J., and Li, B. (2015). The mediodorsal thalamus drives feedforward inhibition in the anterior cingulate cortex via parvalbumin interneurons. J. Neurosci. 35, 5743–5753. https://doi.org/10.1523/JNEUROSCI.4565-14.2015.

Diamond, M.E., von Heimendahl, M., Knutsen, P.M., Kleinfeld, D., and Ahissar, E. (2008). 'Where' and 'what' in the whisker sensorimotor system. Nat. Rev. Neurosci. 9, 601–612. https://doi.org/10.1038/nrn2411.

Dutch-Belgian Fragile X Consortium (1994). Fmr1 knockout mice: A model to study fragile X mental retardation. Cell 78, 23–33.

Erzurumlu, R.S., and Gaspar, P. (2012). Development and critical period plasticity of the barrel cortex. Eur. J. Neurosci. 35, 1540–1553. https://doi.org/10.1111/j.1460-9568.2012.08075.x.

Espinosa, J.S., and Stryker, M.P. (2012). Development and plasticity of the primary visual cortex. Neuron 75, 230–249. https://doi.org/10.1016/j.neuron.2012.06.009.

Flandin, P., Zhao, Y., Vogt, D., Jeong, J., Long, J., Potter, G., Westphal, H., and Rubenstein, J.L.R. (2011). Lhx6 and Lhx8 coordinately induce neuronal expression of Shh that controls the generation of interneuron progenitors. Neuron 70, 939–950. https://doi.org/10.1016/j.neuron.2011.04.020.

Fox, K., and Wong, R.O.L. (2005). A comparison of experience-dependent plasticity in the visual and somatosensory systems. Neuron 48, 465–477. https://doi.org/10.1016/j.neuron.2005.10.013.

Frangeul, L., Pouchelon, G., Telley, L., Lefort, S., Lüscher, C., and Jabaudon, D. (2016). A cross-modal genetic framework for the development and plasticity of sensory pathways. Nature 538, 96–98. https://doi.org/10.1038/nature19770.

Ghosh, A., and Shatz, C.J. (1993). A role for subplate neurons in the patterning of connections from thalamus to neocortex. Development 117, 1031–1047.

Gu, Z., Eils, R., and Schlesner, M. (2016). Complex heatmaps reveal patterns and correlations in multidimensional genomic data. Bioinformatics 32, 2847–2849. https://doi.org/10.1093/bioinformatics/btw313.

He, M., Tucciarone, J., Lee, S., Nigro, M.J., Kim, Y., Levine, J.M., Kelly, S.M., Krugikov, I., Wu, P., Chen, Y., et al. (2016). Strategies and Tools for Combinatorial Targeting of GABAergic Neurons in Mouse Cerebral Cortex (NEURON). https://doi.org/10.1016/j.neuron.2016.08.021.

Hensch, T.K. (2005). Critical period plasticity in local cortical circuits. Nat. Rev. Neurosci. 6, 877–888. https://doi.org/10.1038/nrn1787.

Hoerder-Suabedissen, A., Wang, W.-Z., Lee, S., Davies, K.E., Goffinet, A.M., Rakić, S., Parnavelas, J., Reim, K., Nicolić, M., Paulsen, O., and Molnár, Z. (2009). Novel markers reveal subpopulations of subplate neurons in the murine cerebral cortex. Cereb. Cortex 19, 1738–1750. https://doi.org/10.1093/cercor/bhn195.

Kanold, P.O., and Luhmann, H.J. (2010). The subplate and early cortical circuits. Annu. Rev. Neurosci. 33, 23–48. https://doi.org/10.1146/annurev-neuro-060909-153244.

Kanold, P.O., and Shatz, C.J. (2006). Subplate neurons regulate maturation of cortical inhibition and outcome of ocular dominance plasticity. Neuron 51, 627–638. https://doi.org/10.1016/j.neuron.2006.07.008.

Kanold, P.O., Kara, P., Reid, R.C., and Shatz, C.J. (2003). Role of subplate neurons in functional maturation of visual cortical columns. Science 301, 521–525. https://doi.org/10.1126/science.1084152.

Kohara, K., Pignatelli, M., Rivest, A.J., Jung, H.-Y., Kitamura, T., Suh, J., Frank, D., Kajikawa, K., Mise, N., Obata, Y., et al. (2014). Cell type-specific genetic and optogenetic tools reveal hippocampal CA2 circuits. Nat. Neurosci. 17, 269–279. https://doi.org/10.1038/nn.3614.

Kuhlman, S.J., Olivas, N.D., Tring, E., Ikrar, T., Xu, X., and Trachtenberg, J.T. (2013). A disinhibitory microcircuit initiates critical-period plasticity in the visual cortex. Nature 501, 543–546. https://doi.org/10.1038/nature12485.

Le Magueresse, C., and Monyer, H. (2013). GABAergic interneurons shape the functional maturation of the cortex. Neuron 77, 388–405. https://doi.org/10.1016/j.neuron.2013.01.011.

Lee, S.H., Kwan, A.C., Zhang, S., Phoumthipphavong, V., Flannery, J.G., Masmanidis, S.C., Taniguchi, H., Huang, Z.J., Zhang, F., Boyden, E.S., et al. (2012). Activation of specific interneurons improves V1 feature selectivity and visual perception. Nature 488, 379–383. https://doi.org/10.1038/nature11312.

Li, H., Fertuzinhos, S., Mohns, E., Hnasko, T.S., Verhage, M., Edwards, R., Šestan, N., and Crair, M.C. (2013). Laminar and columnar development of barrel cortex relies on thalamocortical neurotransmission. Neuron 79, 970–986. https://doi.org/10.1016/j.neuron.2013.06.043.

Li, N., Chen, T.-W., Guo, Z.V., Gerfen, C.R., and Svoboda, K. (2015). A motor cortex circuit for motor planning and movement. Nature 519, 51–56. https://doi.org/10.1038/nature14178.

Maffei, A., Nataraj, K., Nelson, S.B., and Turrigiano, G.G. (2006). Potentiation of cortical inhibition by visual deprivation. Nature 443, 81–84. https://doi.org/10.1038/nature05079.

Marques-Smith, A., Lyngholm, D., Kaufmann, A.-K., Stacey, J.A., Hoerder-Suabedissen, A., Becker, E.B.E., Wilson, M.C., Molnár, Z., and Butt, S.J.B. (2016). A Transient Translaminar GABAergic Interneuron Circuit Connects Thalamocortical Recipient Layers in Neonatal Somatosensory Cortex. Neuron 89, 536–549. https://doi.org/10.1016/j.neuron.2016.01.015.

Mayer, C., Hafemeister, C., Bandler, R.C., Machold, R., Batista Brito, R., Jaglin, X., Allaway, K., Butler, A., Fishell, G., and Satija, R. (2018). Developmental diversification of cortical inhibitory interneurons. Nature 555, 457–462. https://doi.org/10.1038/nature25999.

Miska, N.J., Richter, L.M., Cary, B.A., Gjorgjieva, J., and Turrigiano, G.G. (2018). Sensory experience inversely regulates feedforward and feedback excitation-inhibition ratio in rodent visual cortex. eLife 7, e38846. https://doi.org/10.7554/eLife.38846.

Muñoz, W., and Rudy, B. (2014). Spatiotemporal specificity in cholinergic control of neocortical function. Curr. Opin. Neurobiol. 26, 149–160. https://doi.org/10.1016/j.conb.2014.02.015.

Murata, Y., and Colonnese, M.T. (2016). An excitatory cortical feedback loop gates retinal wave transmission in rodent thalamus. eLife 5, e18816. https://doi.org/10.7554/eLife.18816.

Nigro, M.J., Hashikawa-Yamasakié, Y., and Rudy, B. (2018). Diversity and connectivity of layer 5 somatostatin-expressing interneurons in the mouse barrel cortex. J. Neurosci. 2415–17. https://doi.org/10.1523/JNEUROSCI.2415-17.2017.

Parikshak, N.N., Swarup, V., Belgard, T.G., Irimia, M., Ramaswami, G., Gandal, M.J., Hartl, C., Leppa, V., Ubieta, L.T., Huang, J., et al. (2016). Genome-wide changes in lncRNA, splicing, and regional gene expression patterns in autism. Nature 540, 423–427. https://doi.org/10.1038/nature20612.

Phillips, J.W., Schulmann, A., Hara, E., Winnubst, J., Liu, C., Valakh, V., Wang, L., Shields, B.C., Korff, W., Chandrashekar, J., et al. (2019). A repeated

molecular architecture across thalamic pathways. Nat. Neurosci. *22*, 1925–1935. https://doi.org/10.1038/s41593-019-0483-3.

Porter, J.T., Johnson, C.K., and Agmon, A. (2001). Diverse types of interneurons generate thalamus-evoked feedforward inhibition in the mouse barrel cortex. J. Neurosci. *21*, 2699–2710. https://doi.org/10.1523/JNEUROSCI.21-08-02699.2001.

Pouchelon, G., Gambino, F., Bellone, C., Telley, L., Vitali, I., Lüscher, C., Holtmaat, A., and Jabaudon, D. (2014). Modality-specific thalamocortical inputs instruct the identity of postsynaptic L4 neurons. Nature *511*, 471–474. https://doi.org/10.1038/nature13390.

Quattrocolo, G., Fishell, G., and Petros, T.J. (2017). Heterotopic Transplantations Reveal Environmental Influences on Interneuron Diversity and Maturation. Cell Rep. *21*, 721–731. https://doi.org/10.1016/j.celrep.2017.09.075.

Reardon, T.R., Murray, A.J., Turi, G.F., Wirblich, C., Croce, K.R., Schnell, M.J., Jessell, T.M., and Losonczy, A. (2016). Rabies Virus CVS-N2c(ΔG) Strain Enhances Retrograde Synaptic Transfer and Neuronal Viability. Neuron *89*, 711–724. https://doi.org/10.1016/j.neuron.2016.01.004.

Roth, M.M., Dahmen, J.C., Muir, D.R., Imhof, F., Martini, F.J., and Hofer, S.B. (2016). Thalamic nuclei convey diverse contextual information to layer 1 of visual cortex. Nat. Neurosci. *19*, 299–307. https://doi.org/10.1038/nn.4197.

Saalmann, Y.B., Pinsk, M.A., Wang, L., Li, X., and Kastner, S. (2012). The pulvinar regulates information transmission between cortical areas based on attention demands. Science *337*, 753–756. https://doi.org/10.1126/science.1223082.

Shepherd, G.M.G., and Yamawaki, N. (2021). Untangling the cortico-thalamocortical loop: Cellular pieces of a knotty circuit puzzle. Nat. Rev. Neurosci. *22*, 389–406. https://doi.org/10.1038/s41583-021-00459-3.

Silberberg, G., and Markram, H. (2007). Disynaptic inhibition between neocortical pyramidal cells mediated by Martinotti cells. Neuron *53*, 735–746. https://doi.org/10.1016/j.neuron.2007.02.012.

Southwell, D.G., Froemke, R.C., Alvarez-Buylla, A., Stryker, M.P., and Gandhi, S.P. (2010). Cortical plasticity induced by inhibitory neuron transplantation. Science *327*, 1145–1148. https://doi.org/10.1126/science.1183962.

Sun, Q., Li, X., Ren, M., Zhao, M., Zhong, Q., Ren, Y., Luo, P., Ni, H., Zhang, X., Zhang, C., et al. (2019). A whole-brain map of long-range inputs to GABAergic interneurons in the mouse medial prefrontal cortex. Nat. Neurosci. *22*, 1357–1370. https://doi.org/10.1038/s41593-019-0429-9.

Tan, Z., Hu, H., Huang, Z.J., and Agmon, A. (2008). Robust but delayed thalamocortical activation of dendritic-targeting inhibitory interneurons. Proc. Natl. Acad. Sci. USA *105*, 2187–2192. https://doi.org/10.1073/pnas.0710628105.

Tasic, B., Menon, V., Nguyen, T.-N., Kim, T.K., Jarsky, T., Yao, Z., Levi, B., Gray, L.T., Sorensen, S.A., Dolbeare, T., et al. (2016). Adult mouse cortical cell taxonomy revealed by single cell transcriptomics. Nat. Neurosci. *19*, 335–346. https://doi.org/10.1038/nn.4216.

Tasic, B., Yao, Z., Graybuck, L.T., Smith, K.A., Nguyen, T.-N., Bertagnolli, D., Goldy, J., Garren, E., Economo, M.N., Viswanathan, S., et al. (2018). Shared and distinct transcriptomic cell types across neocortical areas. Nature *563*, 72–78. https://doi.org/10.1038/s41586-018-0654-5.

Tosches, M.A., Yamawaki, T.M., Naumann, R.K., Jacobi, A.A., Tushev, G., and Laurent, G. (2018). Evolution of pallium, hippocampus, and cortical cell types

revealed by single-cell transcriptomics in reptiles. Science *360*, 881–888. https://doi.org/10.1126/science.aar4237.

Tuncdemir, S.N., Wamsley, B., Stam, F.J., Osakada, F., Goulding, M., Callaway, E.M., Rudy, B., and Fishell, G. (2016). Early Somatostatin Interneuron Connectivity Mediates the Maturation of Deep Layer Cortical Circuits. Neuron *89*, 521–535. https://doi.org/10.1016/j.neuron.2015.11.020.

Tyson, J.A., Goldberg, E.M., Maroof, A.M., Xu, Q., Petros, T.J., and Anderson, S.A. (2015). Duration of culture and sonic hedgehog signaling differentially specify PV versus SST cortical interneuron fates from embryonic stem cells. Development *142*, 1267–1278. https://doi.org/10.1242/dev.111526.

van Versendaal, D., and Levelt, C.N. (2016). Inhibitory interneurons in visual cortical plasticity. Cell. Mol. Life Sci. *73*, 3677–3691. https://doi.org/10.1007/s00018-016-2264-4.

Vogt, D., Hunt, R.F., Mandal, S., Sandberg, M., Silberberg, S.N., Nagasawa, T., Yang, Z., Baraban, S.C., and Rubenstein, J.L.R. (2014). Lhx6 directly regulates Arx and CXCR7 to determine cortical interneuron fate and laminar position. Neuron *82*, 350–364. https://doi.org/10.1016/j.neuron.2014.02.030.

Wall, N.R., De La Parra, M., Sorokin, J.M., Taniguchi, H., Huang, Z.J., and Callaway, E.M. (2016). Brain-Wide Maps of Synaptic Input to Cortical Interneurons. J. Neurosci. *36*, 4000–4009. https://doi.org/10.1523/JNEUROSCI.3967-15.2016.

Wang, Q., Ding, S.-L., Li, Y., Royall, J., Feng, D., Lesnar, P., Graddis, N., Naeemi, M., Facer, B., Ho, A., et al. (2020). The Allen Mouse Brain Common Coordinate Framework: A 3D Reference Atlas. Cell *181*, 936–953.e20. https://doi.org/10.1016/j.cell.2020.04.007.

Wickersham, I.R., Lyon, D.C., Barnard, R.J.O., Mori, T., Finke, S., Conzelmann, K.-K., Young, J.A.T., and Callaway, E.M. (2007). Monosynaptic restriction of transsynaptic tracing from single, genetically targeted neurons. Neuron *53*, 639–647. https://doi.org/10.1016/j.neuron.2007.01.033.

Wickham, H., and Sievert, C. (2016). ggplot2: Elegant graphics for data analysis, Second Edition (Springer). https://doi.org/10.1007/978-3-319-24277-4.

Williams, L.E., and Holtmaat, A. (2018). Higher-Order Thalamocortical Inputs Gate Synaptic Long-Term Potentiation via Disinhibition. Neuron *101*, 91–102.e4. https://doi.org/10.1016/j.neuron.2018.10.049.

Wilson, N.R., Runyan, C.A., Wang, F.L., and Sur, M. (2012). Division and subtraction by distinct cortical inhibitory networks in vivo. Nature *488*, 343–348. https://doi.org/10.1038/nature11347.

Wu, Z., Litwin-Kumar, A., Shamash, P., Taylor, A., Axel, R., and Shadlen, M.N. (2020). Context-Dependent Decision Making in a Premotor Circuit. Neuron *106*, 316–328.e6. https://doi.org/10.1016/j.neuron.2020.01.034.

Yu, J., Hu, H., Agmon, A., and Svoboda, K. (2019). Recruitment of GABAergic Interneurons in the Barrel Cortex during Active Tactile Behavior. Neuron *104*, 412–427.e4. https://doi.org/10.1016/j.neuron.2019.07.027.

Zhang, S., Xu, M., Chang, W.C., Ma, C., Hoang Do, J.P., Jeong, D., Lei, T., Fan, J.L., and Dan, Y. (2016). Organization of long-range inputs and outputs of frontal cortex for top-down control. Nat. Neurosci. *19*, 1733–1742. https://doi.org/10.1038/nn.4417.

Zhang, S., Lv, F., Yuan, Y., Fan, C., Li, J., Sun, W., and Hu, J. (2019). Whole-Brain Mapping of Monosynaptic Afferent Inputs to Cortical CRH Neurons. Front. Neurosci. *13*, 565. https://doi.org/10.3389/fnins.2019.00565.

STAR★METHODS

KEY RESOURCES TABLE

Reagent or resource	Source	Identifier
Antibodies		
Rat anti-RFP; 1:1000	Chromotek	#5f8; RRID:AB_2336064
Chicken anti-GFP; 1:1000	Aves Labs	#1020; RRID:AB_2734732
Rabbit anti-somatostatin; 1:3000	Peninsula Laboratories	T4103; RRID:AB_518614
Goat anti-ChAT; 1:250	Millipore	AB144P; RRID:AB_2079751
Goat anti-CTGF; 1:500	Santa Cruz Biotechnology	sc-14939; RRID:AB_638805
Rabbit anti-TPH2; 1:500	Novus Biologicals	NB100-74555; RRID:AB_1049988
Goat anti-PV 1:3000	Swant	PVG 213; RRID:AB_2721207
Bacterial and virus strains		
rAAV1-DIO-TVA-GFP-N2cG	This paper	from the Addgene plasmid: #175439
rAAV1-flrtDIO-TVA-GFP-N2cG	This paper	from the Addgene plasmid: #175440
EnvA-CVS-N2c-dG-FlpO-mChrerry	K. Ritola, Janelia	N/A
EnvA- CVS-N2c-dG-H2B:tdTomato	This paper: in house, K. Ritola, Janelia	from the Addgene plasmid: #175441
Deposited data		
Allen Mouse Brain Common Coordinate Framework	Allen institute	https://atlas.brain-map.org/; RRID:SCR_020999
Atlas of the developing mouse brain	Paxinos; Halliday; Watson; Koutcherov; Wang	Elsevier
Experimental models: Organisms/strains		
B6.129P2-Pvalb$^{tm1(cre)Arbr}$/J	The Jackson Laboratories	RRID:IMSR_JAX:017320
Ssttm2.1(cre)^{Zjh}/J	The Jackson Laboratories	RRID:IMSR_JAX:013044
B6J.Cg-Ssttm3.1(flpo)^{Zjh}/AreckJ	The Jackson Laboratories	RRID:IMSR_JAX:031629
B6;CBA-Tg(Lhx6-icre)1Kess/J	The Jackson Laboratories	RRID:IMSR_JAX:026555
B6.Cg-Gt(ROSA)26Sor$^{tm9(CAG-tdTomato)Hze}$/J	The Jackson Laboratories	RRID:IMSR_JAX:007909
B6;129S4-Gt(ROSA) 26Sor$^{tm3(CAG-tdTomato,-EGFP*)Zjh}$/J	The Jackson Laboratories	RRID:IMSR_JAX:028582
B6.129P2-Fmr1^{tm1Cgr}/J	The Jackson Laboratories	RRID:IMSR_JAX:003025
Recombinant DNA- plasmids		
pAAV-VTKS2-TVA-eGFP-N2cG (DIO)	This paper	Addgene ID: #175439
pAAV-VTKS5-TVA-eGFP-N2cG (flrtDIO)	This paper	Addgene ID: #175440
CVS-N2c(dG)-H2B:tdTomato	This paper	Addgene ID: #175441
pCAG-N2cN	Gift from Ian Wickersham	RRID:Addgene_100801
pCAG-N2cP	Gift from Ian Wickersham	RRID:Addgene_100808
pCAG-N2cG	Gift from Ian Wickersham	RRID:Addgene_100811
pCAG-N2cL	Gift from Ian Wickersham	RRID:Addgene_100812
Software and algorithms		
Adobe Photoshop	Adobe Suite	RRID:SCR_014199
Advanced Normalization Tools (ANTs)	http://www.picsl.upenn.edu/ANTS/	RRID:SCR_004757
Prism	GraphPad	RRID:SCR_002798
R v4.0.3	R project	https://www.r-project.org/
R studio	R Studio	https://rstudio.com/products/ rstudio/download-server/
ComplexHeatmap	(Gu et al., 2016)	DOI: 10.1093/bioinformatics/btw313

(Continued on next page)

Continued

Reagent or resource	Source	Identifier
FactoExtra	Kassambara A.	https://CRAN.R-project.org/package=factoextra
Hmisc	F. Harrell	https://CRAN.R-project.org/package=Hmisc
MATLAB	MathWorks	RRID: SCR_001622
ggplot2	(Wickham and SievertC, 2016)	https://ggplot2.tidyverse.org/
Automatic detection	This paper	DOI: 10.5281/zenodo.5573200 https://github.com/yannicko-neuro/Pouchelon_etal_2021
Brainrender	(Claudi et al., 2020)	https://github.com/jupyter/jupyter/issues/190#issuecomment-721264013

RESOURCE AVAILABILITY

Lead contact

Further information and requests for resources and reagents should be directed to and will be fulfilled by the lead contact, Gord Fishell (gordon_fishell@hms.harvard.edu).

Materials availability

Plasmids designed for this paper and used for rAAV and for N2cRV production are now available at Addgene.

Data and code availability

- All quantified data are available in main, supplemental figures, and supplementary tables. All original physiological, imaging, histological data are archived at Harvard Medical School Fishell lab Server.
- The custom MATLAB scripts train the neural network and demonstrate how to perform the slice to atlas matching. Data to train the neural network is included in the repository. Code for the automatic detection program is available on Github: https://github.com/yannicko-neuro/Pouchelon_etal_2021 and archived at Zenodo: https://doi.org/10.5281/zenodo.5573200.
- Any additional information required to reanalyze the data reported in this work paper is available from the lead contact upon request.

EXPERIMENTAL MODEL AND SUBJECT DETAILS

Mice

All experiments were approved by and in accordance with Harvard Medical School IACUC protocol number IS00001269. Animals were group housed and maintained under standard, temperature-controlled laboratory conditions. Mice were kept on a 12:12 light/dark cycle and received water and food *ad libitum*. C57BL/6 mice were used for breeding with transgenic mice. Transgenic mice, PV-Cre (stock number: 017320), SST-Cre (stock number: 013044), SST-FlpO (stock number: 031629), Lhx6-iCre (stock number: 026555), Ai9 (expressing tdTomato, stock number: 007909) and IS reporter (stock number: 028582); Fmr1 KO (stock number: 003025) are available at Jackson Laboratories. For experiments during development, mice were injected at P0, and experiments conducted between ages P3-P15. In the case of adults, mice were injected at P30 or P40, and experiments conducted between ages P42-P52. Both female and male animals were used for all experiments except for the Fmr1 KO mice that were all males.

METHOD DETAILS

Sensory deprivations

To deprive mice from whisker and visual sensory input, infraorbital nerve section (IONS) and enucleation were performed as previously described (Frangeul et al., 2016). P0 mouse pups were anesthetized by hypothermia. For IONS, a unilateral skin incision was made between the eye and the whisker pad, and the infraorbital nerve, which innervates the whisker pad, was carefully cut with a sterile blade. For enucleation, a small incision was made between the eyelids with a scalpel and the eye was separated from the optic nerve with micro-scissors in order to be removed from the orbit with forceps. The pups were allowed to recover on a heating pad before being returned to their mother.

Histology

Mice at between P42-P46 for the adult time point or P10 for the developmental time point (n = 3 or 4 for each condition) were perfused with 4% paraformaldehyde (PFA) and brains were fixed overnight in 4% PFA at 4 °C. 50-μm vibratome sections were used for all histological experiments. Every 4th section was collected for the representation of each brain and the sections were processed for immunohistochemistry in order to confirm somatostatin identity, but also to amplify weak signals that could come from low levels of TVA expression.

For the immunofluorescence, brain sections were incubated 1 h at room temperature in a blocking solution containing 3% Normal Donkey serum and 0.3% Triton X-100 in PBS and incubated overnight or 48hrs at 4°C with primary antibodies: rat anti-RFP (1:1,000; Chromotek #5f8), chicken anti-GFP (1:1,000; Aves Labs #1020), rabbit anti-somatostatin (1:3,000; Peninsula Laboratories International T-4103.0050), goat anti-ChAT (1:250; Millipore AB144P), goat anti-CTGF (1:500; Santa Cruz Biotechnology sc-14939), rabbit anti-TPH2 (1:500, Novus Biologicals NB74555). Sections were rinsed three times in PBS and incubated for 60–90 min at room temperature or overnight at 4°C with the Alexa Fluor 488-, 594- or 647-conjugated secondary antibodies (1:500; Thermo Fisher Science or Jackson ImmunoResearch).

Rabies tracing

For adult mice, stereotactic injections were performed between P30-P35. recombinant AAV-DIO-helpers and N2cRV were diluted at a ratio 1:3 and 23nl were microinjected using NanojectIII at 1nl/second according to stereotaxic coordinates (from Bregma. AP+1.5, ML-0.7, DV-0.85 for ALM; AP −1, ML-3, DV-0.89 for S1; AP-3, ML-2.5, DV-0.50 for V1). Animals were perfused 9-12 days later. For postnatal time points stereotaxic injections were possible using a neonate adaptor (Harvard apparatus). Mouse pups were anesthetized by hypothermia and stereotaxically micro-injected with the rAAV-DIO or fDIO-helpers at P0 (from Lambda AP+1.56, ML-0.56, DV-0.25 for ALM; AP+1.2, ML-1.8, DV-0.2 for S1; AP+0.2, ML-1.66, DV-0.08 for V1) and separately with the N2cRV at P5 (from Lambda AP+2.6, ML-0.56, DV-0.3 for ALM; AP+2, ML-2, DV-0.25 for S1; AP+0.5, ML-2, DV-0.08 for V1). Animals were perfused 5 days later at P10. All coordinates were determined to target mainly the deeper layer (5-6) of the cortex.

Viruses

rAAV1-DIO-helpers (Cre-ON helpers). Titer: 2.1E+09vg/μl. N2cG protein was cloned instead of B19G from the helpers insert of the previously published TVA-eGFP construct (Kohara et al., 2014). This construct was designed from our unpublished 'VTKS2 backbone' (Addgene# 170853), which has DIO sites, but also contains with less restriction sites, a small WPRE and human Synapsin promoter to reduce the total length of the genome and for a high neuronal expression. Now available at Addgene as VTKS2-TVA-eGFP-N2cG (Addgene #175439).

rAAV1-flrtDIO-helpers (Cre-ON, Flp-OFF helpers). Titer: 1.6E+09vg/μl. The construct was built from our unpublished 'VTKS5 backbone' (Addgene #170856): deleting-FRT sites were added around the Lox sites of Cre-ON construct, to trigger whole insert deletion upon FlpO expression. Now available at Addgene as VTKS5-TVA-eGFP-N2cG (Addgene #175440).

Rabies. EnvA-pseudotyped CVS-N2c(deltaG)-FlpO-mCherry was used. Titer: 3.7E+09U/ml. In addition, to simplify automatic detection of cells, we generated Rabies with nuclear expression of reporter. Titer: 1.4E+08U/ml: tdTomato with a nuclear localization signal (H2B:tdtomato) was cloned instead of tdTomato into RV CVS-N2c(deltaG-tdTomato) plasmid previously published (Reardon et al., 2016) and a gift from T. Jessell as Addgene #73462. This new construct is available at Addgene as CVS-N2cdG-H2B:tdtomato (Addgene #175441). Both rabies types were either produced, amplified and EnvA-pseudotyped in lab or generously shared by K. Ritola.

All and analogous afferent description

Afferents were either organized into regions as defined by the atlas (Cortex: ACA- cingulate, ORB - orbital, ALM – anterolateral motor, RSP - retrosplenial, S1 – primary somatosensory, S2 – secondary somatosensory, V1 – primary visual, V2 – secondary visual, AU - auditory, ENT - entorhinal, CL- claustrum, M1 – primary motor; Thalamic nuclei: dLG – dorsal lateral geniculate, LP – lateral posterior, VB- ventrobasal, PO - posterior, AD - anterodorsal, LD - laterodorsal, AV – anteroventral, MD - mediolateral, CM/CL/PCN – centromedian/central lateral/paracentral, Re/RH – reuniens/rhomboid, VAL – ventral anterior lateral, AM - anteromedial, VM -ventromedial; Basal Forebrain: MS – medial septum, DBN – diagonal band, NB – nucleus basalis, Hypothalamus: PA – preoptic area, Raphe, Midbrain: MRN – mesencephalic reticular, AMY - amygdala) either grouped in analogous connectivity.

Analogous connectivity was defined by grouping brain regions based on their common hierarchy and/or function within specific pathways:

Cortex_local = ALM, S1 or V1 respectively; Cortex_contra = all contralateral neurons; Cortex_other = all ipsilateral cortex except local; Cortex_primary = (primary sensory areas: M1, S1, V1, AU) - local connectivity (S1 or V1); Cortex_associative = Cortex_other - Cortex_primary; Subplate = neurons in local cortex located in L6b; Thalamus = whole thalamus; Thalamus_FO = First order nuclei: dLG, VB, LD, AV, VAL; Thalamus_HO = Higher order nuclei: LP, PO, VM, MD; Thalamus_lb = Limbic nuclei: Pf, AD, CM/CL/PCN, Rhe/ RH). Hierarchical functional organization of the thalamus in FO/HO was shown to be reflected by the genetic identity of thalamic nuclei (Phillips et al., 2019) and that as early as P0 during development (Frangeul et al., 2016). RNaseq analysis of the whole thalamus therefore allowed us to identify thalamic nuclei in each of those categories (Figure S2).

Imaging and data analysis

Each brain section containing labeled cells was acquired as a tiled image on a motorized Zeiss Axio Imager A1. Brains with no helper expression were used as controls for pseudotyping and specificity of the EnvA-N2cRV (data not shown). Starter cells (colocalization of GFP[+] helpers and tdTomato[+] N2cRV) were manually quantified on Adobe Photoshop software. Representative brains with less than 10 starter cells were discarded. The highest concentration of starter cells was in deeper layers for all brains (L5-6. Extended Data Figure 1A).

RV[+] retrogradely labeled cells were registered for each region of the Allen Reference Brain atlas for adult brain and of the "Atlas of Developing Mouse Brain at P6" from George Paxinos 2006.

For the automatic detection, we aligned the histological sections to the 3D Allen Mouse Brain Atlas both in adult and development (Wang et al., 2020). We first manually determined the corresponding coronal sections of the atlas to the histological sections. The sections were then matched using the *Advanced Normalization Tools* software (ANTs) (Avants et al., 2014). We used three consecutive steps with decreasing rigidity (rigid, affine, syn). At each of these steps, a down-sampling scheme (8,6,4,2,1x) with Gaussian smoothing (8,6,4,2,1x) was employed until we reached the convergence criterion using mutual information as our metric. To visualize the accuracy, we drew borders according to the Allen Mouse Brain Atlas on the matched histological section.

To automatize the cell counting we first manually segmented 350 fields of view per channel of 78 × 78 pixels, containing at least once cell to generate a ground truth. We then fed these into a neural network using dilated convolutions (dilation factor 1,2,3,4), data augmentation (shear 10% and scaling 15%) and dropout layers to reduce overfitting. We used stochastic gradient descent as our loss functions and the inverse frequency of label counts was used as class weights in the pixel classification layer for the semantic segmentation. The network was trained for 15 epochs after, after which the loss stabilized. During the final iterations the network achieved a 98,8% accuracy. Finally, we plotted all detected cells per histological sections on top of the original image and removed false positives and added missing cells. The position of each cell was then mapped onto the Allen Mouse Brain Atlas to get a counting of cells per region.

Multiple regression analysis with dummy variables (factors cell types, areas, time points) was performed in R using the 'lm' function and F values/p values analyzed with 'anova' function.

Principal component Analysis (PCA) and follow-up k-means clustering (with numbers of contributing factors determined at 3) was generated using 'FactorExtra'. All heatmaps were generated using the 'ComplexHeatmap' package in R.

ANOVA and t test analysis were performed using Prism (GraphPad). Statistical significance was tested with non-paired, two-sided t test, with a 95% confidence interval. The data distribution was assumed to be normal based on previous studies (Ährlund-Richter et al., 2019), but this was not formally tested. To test for cell type or areal-specificity, values in bar graph were first tested with one-way ANOVA tests followed by the post hoc Tukey multiple comparison test. To test developmental changes within each condition, a Student's t test was applied. All values in bar graphs are expressed as mean ± sem. Circles in bar graphs denote individual animals.

In vitro electrophysiology

P10-11 mice for development and P40-P45 mice for adult time points were used for electrophysiology experiments. Mice anaesthetized with halothane were decapitated and the dissected brains were immersed in ice cold oxygenated (95%O_2 / 5% CO_2) sucrose cutting solution of the following composition 87 mM NaCl, 2.5 mM KCl, 2 mM MgCl2, 1 mM CaCl2, 1.25 mM NaH2PO4, 26 mM NaHCO3, 10 mM glucose and 75 mM sucrose (pH 7.4). 300um thick coronal slices containing ALM, S1 and V1 were cut using Leica VT 1200S vibratome. Slices were incubated in a holding chamber in aCSF of following composition 125 NaCl, 20 Glucose, 2.5 KCl, 1.25 NaH2PO4, 26 NaHCO3, 2 CaCl2, 1MgCl2 (pH = 7.4) for 30 min at 34°C and then for 45 mins at room temperature. For recording, slices were transferred to recording chamber where SST and PV cINs were identified under an upright differential interference contrast microscope (BX51WI) using a 40 × objective (water immersion lens, 0.9 numerical aperture). To visualize SST versus PV cINs, MIGHTEX LED attached to the upright microscope was used. During recording slices were continuously perfused with oxygenated acsf (95%O_2 / 5% CO_2) at a flow rate of 1ml/min at room temperature.

For whole cell patch clamp recording, 5-7 MΩ pipettes were pulled from thick-walled borosilicate glass capillaries on a P-1000 Flaming Micropipette Puller (Sutter Instrument). The pipettes were filled with internal solution of the following composition: 130 K-Gluconate, 10 KCl, 10 HEPES, 0.2 EGTA, 4 MgATP, 0.3 NaGTP, 5 Phosphocreatine and 0.4% biocytin (pH = 7.3).

Recordings were performed using a Multiclamp 700B amplifier and digitized using Digidata 1440A using a sampling rate of 20KHz. Series resistance was continuously monitored during the recording and cells were discarded if the series resistance was > 40MOhms or if it changed by > 20% during the recording. For measurement of intrinsic properties, cells were held at −70mV. No liquid junction potential correction was made. Intrinsic cellular properties of visually identified PV and SST cINs were measured in current clamp mode. Resting Membrane Potential (RMP) of the cell was recorded as mean membrane potential from a 1 min long recording in I = 0 mode. Input Resistance (IR) was computed using Ohm's law (V = I/R) by finding the slope of the IV curve obtained using current injection from −10 to 10pA in steps of 5pA. Highest firing frequency was computed as the maximum firing frequency of a cell for any input current from −100 to 400pA. Rheobase was defined as the minimum input current to evoke firing from a cell. Action potential kinetics were computed from the first spike produced by the cell when a series of increasing input currents were injected. Spike threshold was defined as the membrane potential where dv/dt > 5mV/ms before spike initiation. Action potential half width is defined as the width of an action potential at half of the peak value from spike threshold. Spike Frequency Adaptation (SFA) Is calculated as ISIfirst/ISIlast. Fast hyperpolarization (fAHP) is calculated as the difference between spike threshold and minimum voltage after the

spike within 10ms. mAHP is defined as difference between spike threshold and minimum voltage after the spike, from 10 to 20ms. All analysis was done using clampfit and Easy electrophysiology. Statistical analysis was done in GraphPad prism 9.

QUANTIFICATION AND STATISTICAL ANALYSIS

No prior test for determining sample size was conducted. The data distribution was assumed to be normal based on previous studies (Ährlund-Richter et al., 2019), but this was not formally tested. All statistical analysis were performed using Prism (GraphPad), except for multiple regression analysis performed in R with 'lm' and 'anova' functions. Statistical significance was tested with either ANOVA, followed by multiple comparison Tukey's test or non-paired, two-sided t test, with a 95% confidence interval. To test for cell-type or areal specificity, values in bar graph were first tested with one-way ANOVA tests followed by the post hoc Tukey multiple comparison test. To test developmental changes within each condition, a Student's t test was applied. All statistical details can be found both in the results and the legends of the corresponding figure. N represent the number of animals, while n represent the number of cells. All data are represented as s mean ± SEM.